ARTICLES
https://doi.org/10.1038/s41928-020-0459-z
nature electronics

A generic electroluminescent device for emission from infrared to ultraviolet wavelengths

Yingbo Zhao[1,2,3], Vivian Wang[1,2,3], Der-Hsien Lien[1,2,3] and Ali Javey[1,2] ✉

The range of luminescent materials that can be used in electroluminescent devices is limited due to material processing challenges and band alignment issues. This impedes the development of electroluminescent devices at extreme wavelengths and hinders the use of electroluminescence spectroscopy as an analytical technique. Here, we show that a two-terminal device that uses an array of carbon nanotubes as the source contact can excite electroluminescence from various materials independent of their chemical composition. Transient band bending, created by applying an a.c. gate voltage, is used to achieve charge injection across different band alignments. As a result, the device can produce electroluminescence from long-wave infrared (0.13 eV) to ultraviolet (3.3 eV) wavelengths depending on the emitting material drop-casted on top of the nanotube array, and with onset voltages approaching the optical energy gap of the emitting material. We show that our device can be used to probe a chemical reaction in a liquid droplet via electroluminescence spectroscopy and can be used as an electroluminescence sensor for detecting organic vapours.

Electroluminescence (EL) is fundamental to the operation of light-emitting devices and encodes compositional information of the emitting material that can be analysed by EL spectroscopy. To achieve EL emission, devices adopt different structures, operate with different mechanisms and have emitters of different compositions[1–6]. However, they typically require particular features to accommodate different emitting materials, as the generation of EL requires the injection and radiative recombination of oppositely charged carriers into the emitting layer.

Common d.c. inorganic and driven organic light-emitting diodes (OLEDs) rely on either p- and n-doped regions or multiple charge-transport layers designed to have proper band alignment with the emitter layer[2,4]. Light-emitting electrochemical and electrochemiluminescence cells depend on electrochemical processes, which require the presence of an ionic component or electrolyte in the emitting layer[7,8], to generate EL. A.c.-driven EL devices do not necessarily require emitter-specific charge-injection layers[7–11]. However, early examples (such as sulfide-based light-emitting capacitors) require high operation voltages of over 100 V to achieve impact excitation or bipolar field emission[11,12]. Organic a.c.-driven light-emitting devices have recently been shown to operate at lower voltages while maintaining high brightness, but still apply voltages well beyond the optical band gap of the emitting material[6,9,13,14].

A device that can excite EL directly from a wide variety of emitters of different morphologies, compositions and emission wavelengths has not yet been achieved. However, such a device could enable the broader use of EL spectroscopy as a material analysis technique and accelerate the development of light-emitting devices at extreme wavelengths. To fabricate a generic EL device, two key challenges need to be addressed. First, the deposition of the emissive material should be the last step of the fabrication process. For many molecular systems, either the emitter layer would be damaged by additional processing, or the emitter layer cannot be deposited as a uniform thin film for the deposition of subsequent layers (for example, a droplet of solution). There is also a minimum thickness of the emitter layer required in conventional OLEDs, with nanometre-thick films being incompatible due to pinhole formation. Second, the device structure must allow for carrier injection into a broad range of materials, including those with large energy barrier heights or mobilities approaching zero. Current OLEDs require optimization of multiple injection layers for each corresponding emitter material, which limits the range of wavelengths that can be excited by any single device.

In this Article, we report an a.c.-driven metal–oxide–semiconductor (MOS) capacitor structure with a carbon nanotube (CNT) network source contact that allows carrier injection in arbitrary emissive materials deposited on top of the device (Fig. 1). Instead of relying on specific charge-injection layers, band bending induced at the interface between the CNTs and emitting layer by the a.c. voltage allows efficient bipolar charge injection to be attained regardless of the barrier heights between the contact and the emissive material[15]. Critically, the dense CNT network allows charge injection into emissive materials with low carrier mobility. The bottom gate contact, gate oxide layer and source contact of this structure can be fabricated before the deposition of the emitter layer. The emissive material can be deposited on top of the prepared substrate without any subsequent processing (Supplementary Fig. 1). By removing limits on the emitter material's processability and band alignment between layers, our generic device can generate EL from a wide range of materials with peak emission from ultraviolet (3.3 eV) to long-wave infrared (0.13 eV) wavelengths. We illustrate the potential of the approach for EL spectroscopy by probing the dynamics of an imine condensation reaction occurring in a droplet of liquid on the device, and also show that the device can be used as a chemical sensing platform for organic vapours.

Device structure and EL from different materials

To fabricate the EL device, semiconducting CNTs are assembled on a 50-nm SiO_2/p^{++} Si substrate through a solution-processing method[16]. The CNTs deposited in this way form a continuous network that is conductive (sheet resistance ~80 $k\Omega\,sq^{-1}$) but also highly porous. Varying the CNT assembly time gives different CNT

---

[1]Electrical Engineering and Computer Sciences, University of California at Berkeley, Berkeley, CA, USA. [2]Materials Sciences Division, Lawrence Berkeley National Laboratory, Berkeley, CA, USA. [3]These authors contributed equally: Yingbo Zhao, Vivian Wang, Der-Hsien Lien. ✉e-mail: ajavey@eecs.berkeley.edu

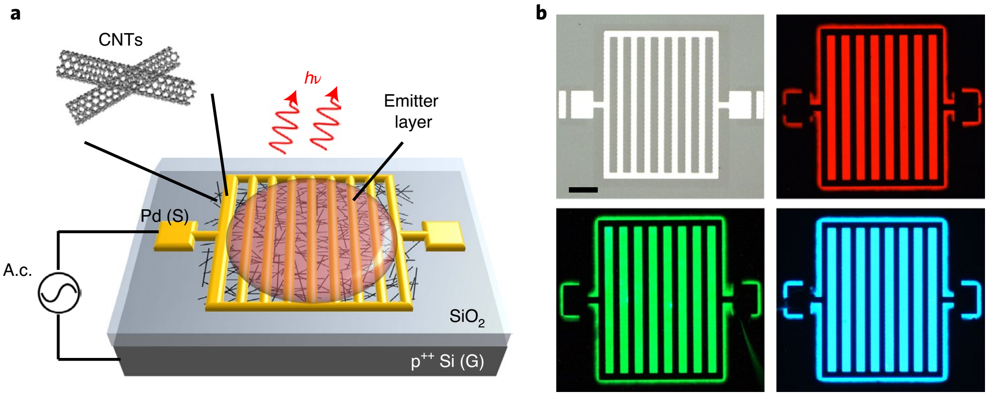

Fig. 1 | Device structure and EL image. a, The device structure with an assembled CNT network on SiO$_2$/Si and patterned source contact. The device operates by applying a.c. voltage between the metal grid on the CNT network (S) and Si backgate (G). **b**, Uniform EL can be excited with all types of emitter, where Ru(bpy)$_3$(PF$_6$)$_2$ (**2**), CdSSe/ZnS alloyed quantum dots (520 nm) and PFO (**1**) are used as red, green and blue emitters in the EL image. Devices are measured with a 15-V, 100-kHz square wave. Scale bar, 0.1 mm.

densities (Supplementary Fig. 2). Although the CNT network is the source contact, a metal grid electrode is patterned by photolithography for wire-bonding and to reduce the parasitic resistance (Supplementary Fig. 1a). The CNT network outside the metal grid area is etched with O$_2$ plasma (Supplementary Fig. 1b). A field-effect transistor is fabricated next to each EL device to check the electrical properties of the CNT network (Supplementary Fig. 3). We chose semiconducting CNTs instead of metallic CNTs because the former can be uniformly assembled over large areas with poly-L-lysine, but metallic CNTs can also be used as contacts to produce EL (Supplementary Fig. 4). It is worth noting that CNTs have previously been used as additives in light-emitting layers of a.c. organic light-emitting devices to enhance device brightness[9,17,18], and CNT networks have also been used as source contacts in a light-emitting transistor to allow for gate control in a vertically structured, multilayer device[19]. The light-emitting materials are deposited on the CNT network contact by drop-casting, spin-coating or evaporation, and a.c. voltage is applied to the gate while grounding the metal contact grid, which contacts the CNT network. Uniform EL can be obtained with different types of material at different wavelengths, as shown by the EL images of poly(9,9-dioctyl-9H-fluorene-2,7-diyl) (PFO, **1**, conjugated polymer), CdSSe/ZnS alloy quantum dots (520 nm; inorganic semiconductor) and Ru(bpy)$_3$(PF$_6$)$_2$ (**2**, fluorescent molecule) in Fig. 1b. As the device does not impose any requirements on the processability of the emitters, a wide variety of materials can be used, from small molecules that form scattered crystals to polymers that form glassy films. Moreover, the device does not rely on emitter-specific charge-injection layers and therefore does not limit the choice of emitters with regard to the achievable band alignment between layers. These advantages allow for the production of EL from the long-wave infrared to ultraviolet range (Fig. 2a). Specifically, 2,7-di-*tert*-butylpyrene (BPYE, **3**) gives EL up to the ultraviolet region, PFO and CdSSe/ZnS alloy quantum dots (520 nm) give blue and green emission and Ru(bpy)$_3$(PF$_6$)$_2$ (**2**), PbS quantum dots and HgTe[20] quantum dots give red, short-wave infrared and mid- to long-wave infrared emission, respectively. Notably, small aromatic molecules such as pyrene and anthracene, which possess highest occupied molecular orbital–lowest unoccupied molecular orbital (HOMO–LUMO) gaps corresponding to the ultraviolet region, have not been reported in OLEDs due to difficulties in band alignment with selective charge-injection layers and their strong tendency to crystallize into non-uniform films. For HgTe quantum dots emitting in the mid- to long-wave infrared regime, the EL is absorbed by most organic materials and can only be observed when the emitting layer is the top layer of the device, likewise preventing their incorporation in conventional OLEDs. With the device reported herein, we produce EL from materials of all types, from colloidal nanomaterials such as quantum dots (Fig. 2b) to aromatic molecules (Fig. 2c), conjugated polymers (Fig. 2d) and metal complexes (Fig. 2e). For simplicity, we only show three or four emitters per material type; more examples can be found in Supplementary Information in comprehensive tables of emitters used on the device (Supplementary Tables 1–4). With such a generic EL device, multiplexed EL from different materials can be achieved with an array of the EL devices where each emitting material is deposited on one pixel of the array. We demonstrate multiplexed EL with four different emitters (BPYE (**3**), poly[(9,9-di-(2-ethylhexyl)-9H-fluorene-2,7-vinylene)-co-(1-methoxy-4-(2-ethylhexyloxy)-2,5-phenylenevinylene)] (PFV, **4**), Ru(bpy)$_3$(PF$_6$)$_2$ (**2**) and CdSeTe/ZnS quantum dots 850 nm (IRQDs)), with each emitter belonging to a different class of materials (aromatic molecules, conjugated polymers, molecular metal complexes and inorganic semiconductors) and emitting at a different wavelength in the ultraviolet to infrared region (Fig. 2f and Supplementary Fig. 5). EL of the four different emitters can be simultaneously measured (Fig. 2g) within a 2.25-mm^2 area, demonstrating the potential to use this EL device for multiplexed EL generation. The device area can be scaled up without fundamental limitations as demonstrated by a 25-mm^2 device (Supplementary Fig. 6).

Device simulation and operation mechanism

To better understand the role of the CNT network in enabling light emission from a variety of materials, we performed device simulations on the basis of the structure shown in Fig. 3a, which consists of two parallel grounded CNT source contacts spanned by a light-emitting semiconducting material (Supplementary Information). The simulated emissive material was placed on top of a 50-nm SiO$_2$ layer with a gate contact on the bottom to which a ±15-V pulsed gate voltage (V_g) with finite slew rate was applied (Fig. 3b). As shown in Fig. 3a, this structure represents the region of emissive material between two individual CNTs separated by a distance L on the same plane. Energy band diagrams calculated at steady state and transition points of the pulsed waveform demonstrate the ability to inject electrons and holes into the emissive material from the CNT contacts at upward and downward transitions, respectively (Fig. 3c). At a gate voltage of −15 V, the electron and hole quasi-Fermi levels (E_{Fn} and E_{Fp}) are situated near the valence band (E_V), indicating that a high density of holes is present in the semiconductor at steady state. As the gate voltage sharply increases to +15 V, the hole density rapidly diminishes while the electron

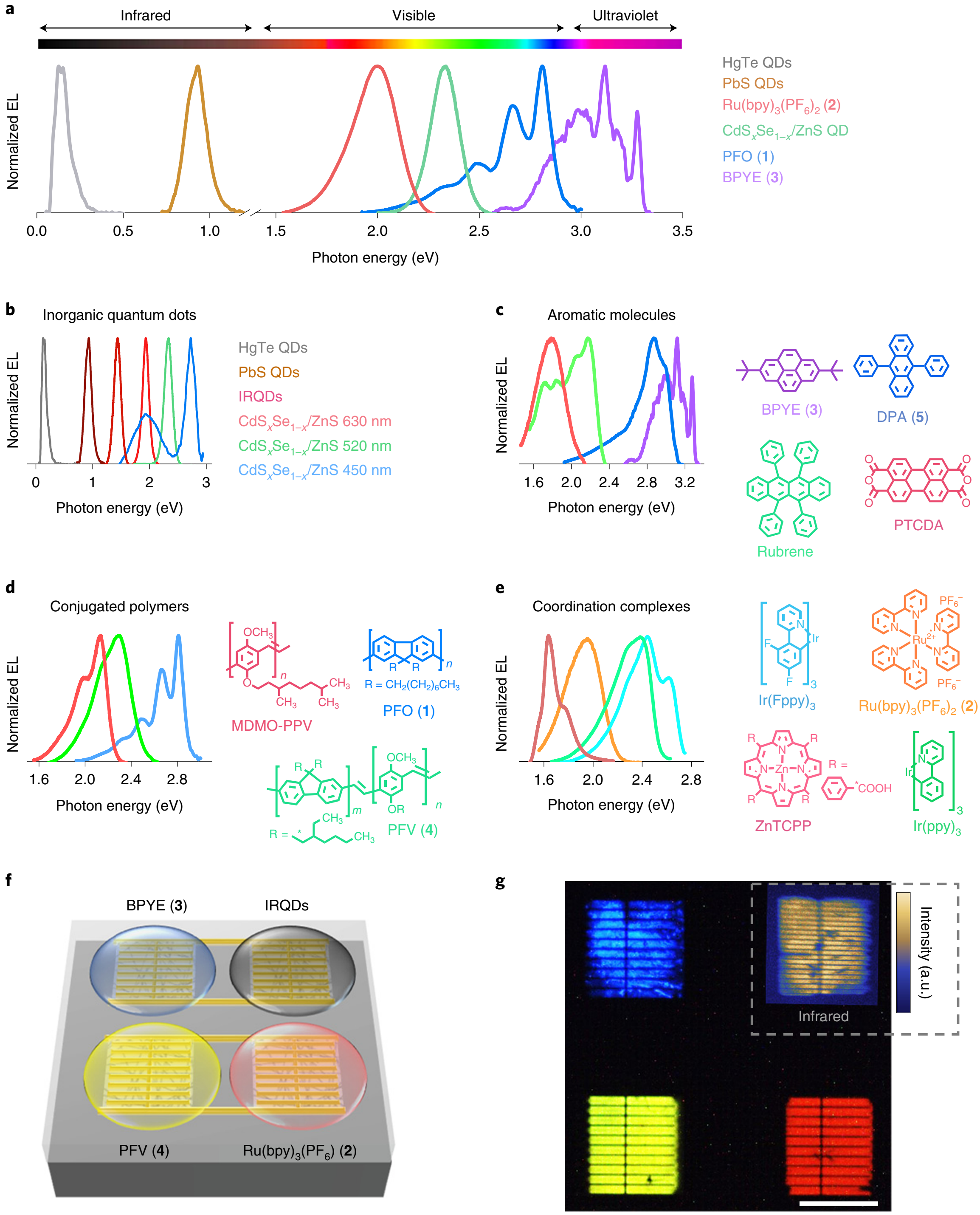

Fig. 2 | EL from long-wave infrared to ultraviolet wavelengths with different types of material. a, EL spectra of the device with different emitting materials from long-wave infrared to ultraviolet regimes. QD, quantum dot. **b–e**, The device can excite EL from a wide variety of materials, including inorganic quantum dots (**b**), aromatic molecules (**c**), conjugated polymers (**d**) and coordination complexes (**e**). PTCDA, perylenetetracarboxylic dianhydride; MDMO-PPV, poly[2-methoxy-5-(3′,7′-dimethyloctyloxy)-1,4-phenylenevinylene]; TCPP, 4,4′,4″,4‴-(porphyrin-5,10,15,20-tetrayl)-tetrabenzoic acid; ZnTCPP, the coordination polymer formed by zinc nitrate and TCPP. **f**,**g**, Different emitting materials can be drop-casted on an array of EL devices (**f**), which produces EL from the infrared to ultraviolet range within a 2.25-mm^2 device area (**g**). a.u., arbitrary units. The emitting materials are BPYE (**3**, ultraviolet to blue), PFV (**4**, yellow), Ru(bpy)$_3$(PF6)$_2$ (**2**, red) and IRQDs (infrared), respectively. The infrared EL image is shown with false colour. Scale bar, 0.5 mm.

density increases, resulting in transient EL as entering electrons recombine radiatively with exiting holes (Fig. 3d–f). EL at the downward transition can be explained similarly and is consistent with previous explanations of a.c. EL[15].

Tunnelling of carriers into the emissive material at voltage transitions is achieved by steep band bending at the resistive Schottky contacts as the electric field across the capacitive structure attempts to switch. Notably, the steep band bending at voltage transitions

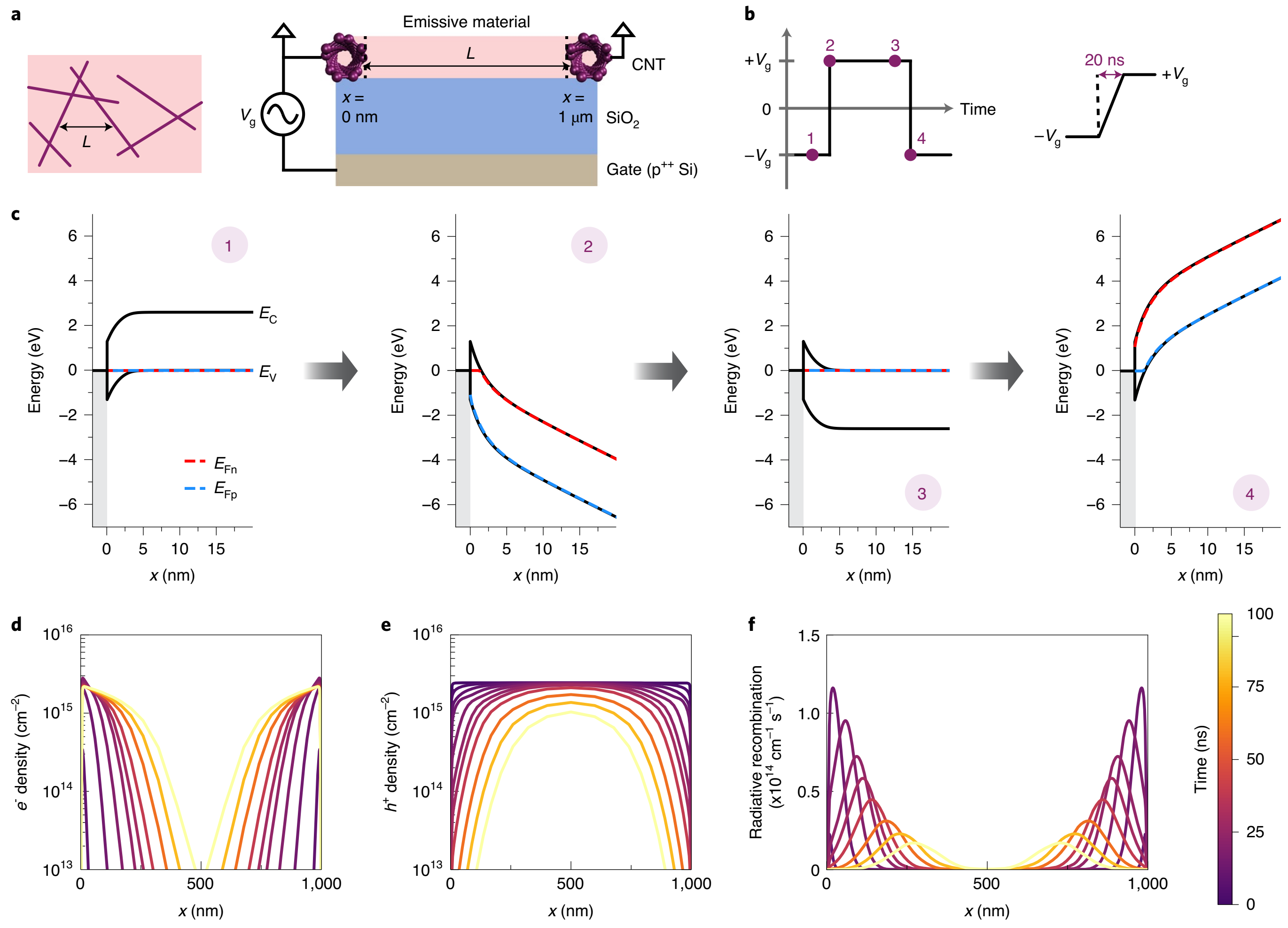

Fig. 3 | Device simulation. a, A schematic of the simulated device structure. The top view (left) shows a random CNT network amongst a layer of emissive material with carrier mobility μ. The cross-sectional view (right) shows the region of emission between two grounded CNT contacts. **b**, A square-wave pulsed voltage is applied to the bottom gate contact with $V_g = 15$ V and a slew rate of 0.75 V ns^{-1}. **c**, Energy band diagrams at one of the source contacts for the timepoints indicated in **b** using a simulated device with 50-nm SiO_2, $\mu = 0.001$ cm^2 V^{-1} s^{-1} and $L = 1$ μm. E_C is the conduction band. The contact is located at $x < 0$ and the emissive material is located at $x > 0$. **d–f**, Electron density (**d**), hole density (**e**) and radiative recombination (**f**) as functions of distance in the channel after an upward transition (that is from time 1 to 2), with colour indicating the time elapsed since the start of the transition.

obviates the need for work-function alignment of the contacts and enables carrier injection and EL even in materials with large injection barriers, as long as a pulse with sufficiently high voltage and slew rate is applied. At the gate voltages considered in this study, carriers can also occupy higher sub-band states of the low-dimensional CNTs, which may promote carrier injection into materials with large band (HOMO–LUMO) gaps (Supplementary Fig. 7).

Device characterization and optimization

We first characterized device performance using $Ru(bpy)_3(PF_6)_2$ (**2**) as a model emitting material. The EL intensity increases with both voltage and frequency (Fig. 4a,b), which is consistent with the a.c. charge-injection mechanism. When applying a square-wave gate voltage with sufficiently low frequency, charge-carrier populations in the emitting material reach steady state before each gate-voltage transition and the average EL intensity increases linearly with frequency, or the number of gate-voltage transitions per unit time (Fig. 4b). The linear relationship between EL intensity and frequency is general to different emitters (Supplementary Fig. 8). EL continues to increase with frequency until the time interval between gate-voltage transitions is not long enough for the device to reach steady state (Supplementary Fig. 9). The pulsed nature of the EL is further confirmed by time-resolved EL measurement (Fig. 4c), where EL is only observed during gate-voltage transients. The difference in EL intensity between the upward and downward transitions reflects the different barrier heights for injection of electrons and holes. The device performance characteristics agree well with our understanding of its operation mechanism and is different from that of light-emitting electrochemical cells or electrochemiluminescence cells. Light-emitting electrochemical cells rely on electrochemical processes at the electrode interface to inject carriers into the emitter, can operate in both a.c. and d.c. modes and have a much longer (milliseconds to hours) turn-on time[7]. Electrochemiluminescent cells operate through electrochemiluminescence, which is a charge transfer reaction between reduced and oxidized forms of luminophores that produces excited states of the molecule and leads to light emission. The EL of electrochemiluminescent cells displays a unique frequency dependence that typically peaks at 1 kHz, which corresponds to the time required to establish electrochemical double layers at the electrode (Supplementary Fig. 10)[21]. Although electrochemiluminescence could take place in the device on the molecular level, as reduced and oxidized species

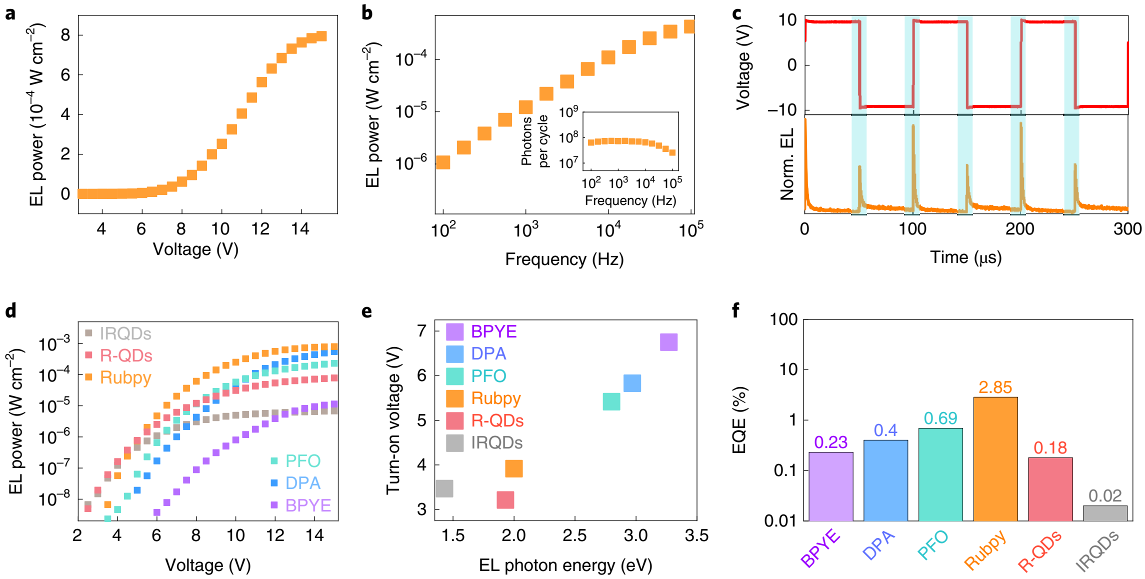

Fig. 4 | Device characterization. a,**b**, The voltage (**a**) and frequency (**b**) dependence of the device EL show characteristics consistent with device simulation. **b**, Inset: the device produces an approximately constant EL per cycle until the frequency is too high for the device to reach steady state. **c**, The operation mechanism is further confirmed by time-resolved EL measurement showing the pulsed nature of EL. **d**,**e**,**f**, The EL intensities, turn-on voltages and EQEs, respectively, of different emitters. The turn-on voltage is defined as the voltage where the EL power density reaches 5×10^{-8} W cm^{-2} (where EL can be accurately measured by the power meter). Rubpy, $Ru(bpy)_3(PF_6)_2$ (**2**), R-QDs, CdSSe/ZnS alloy quantum dots (630 nm). Device measured at 12.5 V for **b** and 100 kHz for **a**,**d**,**e**.

can coexist during the gate-voltage transients, the device characteristic is different from that of electrochemiluminescent cells since the EL linearly increases with frequency to at least 100 kHz.

To better characterize the device performance across a wide variety of emitters, we measured the voltage dependence of EL for six different emitters (BPYE (**3**), 9,10-diphenylanthracene (DPA, **5**), PFO (**1**), $Ru(bpy)_3(PF_6)_2$ (**2**), CdSSe/ZnS alloy quantum dots (630 nm) and IRQDs) from different material categories (inorganic semiconductors, aromatic molecules, conjugated polymers and metal complexes) and with EL wavelengths ranging from ultraviolet to infrared (Fig. 4d and Supplementary Fig. 11). The EL spectrum of each emitter is presented in Fig. 2. It is clear that device operation is not limited to any specific material category, but the stability of the device varies depending on the emitter (Supplementary Fig. 12). For emitters giving visible EL, the emission power can be converted to luminance by considering the luminosity function (Supplementary Table 5). The device turn-on voltage increases with the peak EL photon energy (Fig. 4e). It is worth noting that this trend does not take into account differences in photoluminescence quantum efficiency for different emitters. The external quantum efficiency (EQE) can be estimated by operating the device with a sine-wave a.c. voltage and measuring the EL intensity and current (Methods and Supplementary Fig. 13). The estimated lower limit of the device EQE for various emitter materials is summarized in Fig. 4f, and the EQEs for $Ru(bpy)_3(PF_6)_2$ (**2**), DPA (**5**) and PFO (**1**) are of the same order as their d.c. OLED counterparts[22–24].

We further studied the effect of emitter layer thickness to investigate how much emissive material is required for reasonably bright EL. For this purpose, we used PFO (**1**) as the model emitter as it can be readily spin-coated into uniform films. With PFO (**1**) thickness increasing from 1.5 to 8 nm, the device EL increases linearly with thickness and does not further increase with higher PFO (**1**) thickness (Supplementary Figs. 14 and 15). Remarkably, the device can function with an emitter layer only 1.5 nm thick. This result indicates that the device can be used to obtain EL spectra from small amounts of analyte.

CNT network contacts provide the unique ability to tune the density of contacts to the emissive material. By controlling the assembly time, the average distance *L* between individual nanotubes can be optimized to maximize the time-averaged EL from the emissive material. As *L* increases, the resistance between source contacts increases and the delay in switching the voltage across the capacitive structure becomes longer, lengthening the time during which emission is observed after the transition. At the same time, more area is available for carriers to travel and radiative recombination to occur, increasing the total amount of radiative recombination. When the CNT–CNT distance is too short, gate control of the emissive material channel is weakened and the degree of band bending in the channel is limited, akin to the short-channel effect in transistors. As shown in Supplementary Fig. 16a, the peak amount of radiative recombination increases with increasing *L* up to a certain length, after which the benefit of increasing *L* becomes less important.

Although simulations indicate that large *L* (or sparse CNT networks) is beneficial for improving emission between two single nanotube contacts, the amount of radiative recombination per unit area of the device surface is proportional to both the amount of radiative recombination between two individual contacts and the density of contacts. By approximating the contact density ρ as $1/L^2$ CNTs cm^{-2}, where *L* is the average distance between nanotubes[25], we find that there is an optimal distance between CNT contacts that maximizes the amount of radiative recombination, or EL. Note that the average distance between nanotubes must still be lower than the percolation threshold for an electrically conducting network to form across large areas. Experimental measurements, as discussed in greater detail in the next section, show that devices with very low- or very high-density CNT networks tend to exhibit degraded emission intensity (Supplementary Fig. 16c), thus corroborating our simulation results and demonstrating that device performance can be enhanced by controlling contact density. Importantly, the optimal distance between source contacts depends on the mobility of the semiconducting material (Fig. 5b and Supplementary Fig. 16b); in materials with low mobility, carriers are less able to travel far into

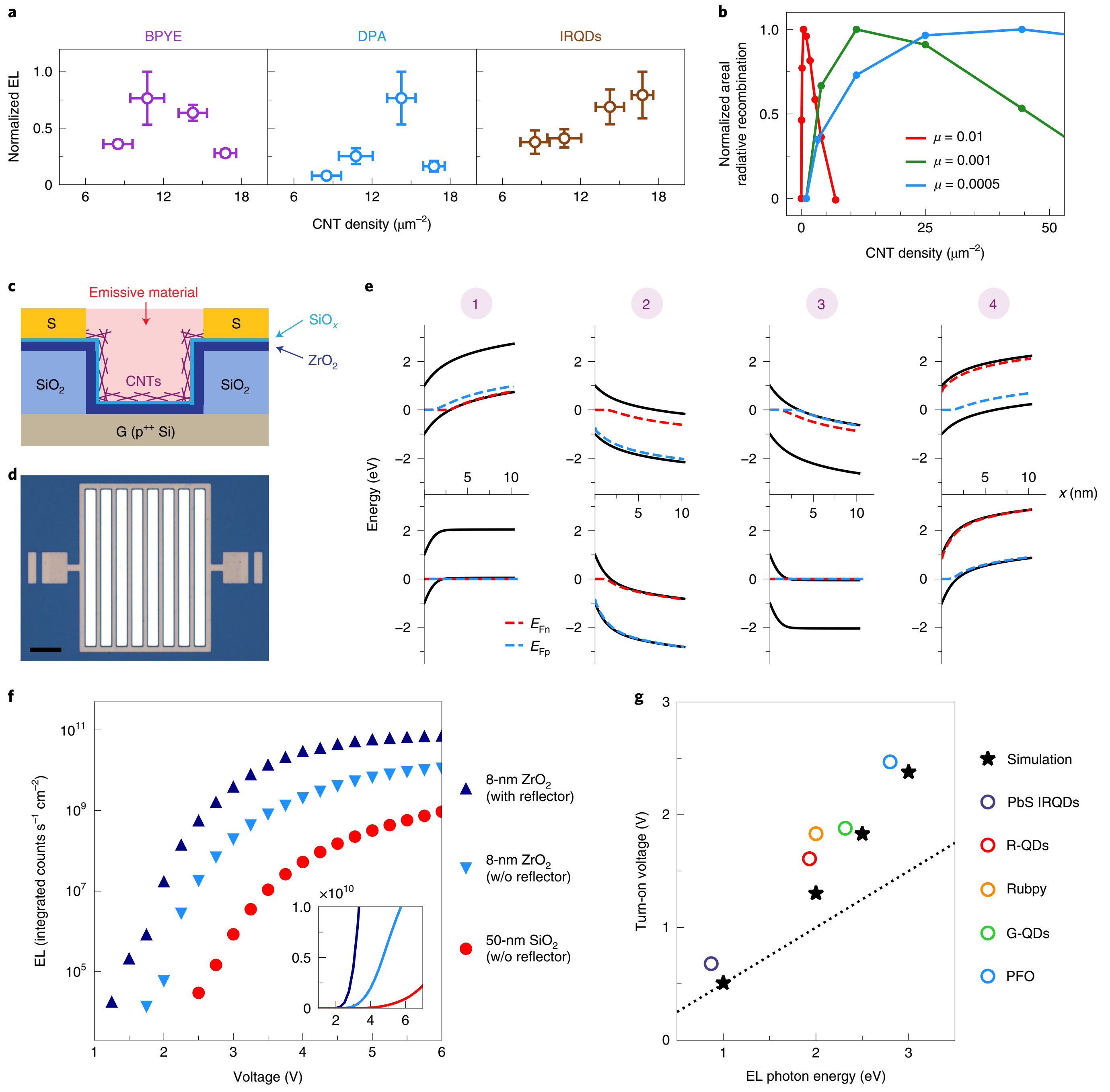

Fig. 5 | Device optimization. **a**, Experimentally measured dependence of EL on semiconducting CNT network density for different emitters. Error bars represent s.d. **b**, Simulated radiative recombination per unit surface area as a function of CNT density for 50-nm SiO_2 gate oxide devices with emitter materials of different mobilities (units $cm^2 V^{-1} s^{-1}$). **c**,**d**, Cross-sectional schematic (**c**) and optical image (**d**) of a device with thin gate dielectric. Scale bar, 100 μm. **e**, Simulated band diagrams at the contact–emitter interface for the same timepoints as in Fig. 3 with $V_g = 3$ V. For each time, the top plot represents a device with 50-nm SiO_2 gate dielectric and the bottom plot represents a device with 8-nm high-*k* (*k*, dielectric constant; relative dielectric constant $\varepsilon = 22$) gate dielectric. **f**, EL from $Ru(bpy)_3(PF_6)_2$ using metallic CNT devices with a gate oxide of 50-nm SiO_2, 8-nm ZrO_2 or 8-nm ZrO_2 on top of an additional back reflector. Inset: data with linear scaling. **g**, Experimentally measured (circles) and simulated (stars) turn-on voltages for different emitters (abbreviations as in Fig. 4, with the addition of the PbS IRQDs and green (G-)QDs). The dotted line marks the gate voltage corresponding to half the photon energy ($V_g = E_{ph}/2$), which represents a total voltage swing of $2V_g = E_{ph}$. Measurements were performed using 8-nm ZrO_2 gate oxide devices without a back reflector.

the emissive material bulk, meaning that it is desirable to increase the contact density, that is reduce the distance between nanotubes, to improve the brightness of emission.

We experimentally studied the dependence of EL on CNT density for six different emitters encompassing inorganic semiconductors, aromatic molecules, conjugated polymers and metal complexes with emission wavelengths from infrared to ultraviolet (Fig. 5a and Supplementary Fig. 16c), where different CNT assembly times were used to fabricate devices with different CNT densities. CNT assembly times of 5, 10, 30 and 60 min gave average CNT densities around

9, 11, 14 and 17 CNTs μm^{-2} respectively, as characterized by atomic force microscopy (Supplementary Fig. 2). The increase in CNT density also results in increased gate capacitance and on-current of CNT field-effect transistor devices consistent with literature values (Supplementary Fig. 3). For $Ru(bpy)_3(PF_6)_2$ (**2**), BPYE (**3**), PFO (**1**) and DPA (**5**), the optimal CNT density was found to be 11 or 14 CNTs μm^{-2}, which can be achieved with assembly times of 10 or 30 min. For the IRQDs, higher CNT density tends to give higher EL. The general trend of CNT density dependence is consistent with device simulation results, further supporting our picture of the operating mechanism. Simulated calculations of radiative recombination as a function of CNT density show that EL in lower-mobility materials can be enhanced by using higher-density CNT contacts (Fig. 5b). In the lowest-mobility case ($\mu = 0.0005\,cm^2\,V^{-1}\,s^{-1}$), EL appears to increase monotonically with CNT density because the optimum in CNT density lies outside the range shown. Thus, it is possible for the EL of certain emitters to appear to strictly increase or remain nearly constant with CNT density depending on properties of the deposited emissive material and the range of CNT densities tested. From a practical perspective, all emitter materials exhibit reasonable EL (more than half the highest EL value measured) with a 30-min-assembled CNT network contact, so it would be possible to obtain EL from different types of material without changing the CNT density on the device.

Finally, we investigated the impact of gate dielectric scaling on EL generation in a.c.-driven devices (Fig. 5c–g), which are conventionally known to suffer from high operating voltages. From both simulation and experimental results (Supplementary Fig. 17), we find that the onset voltage for EL decreases as the SiO_2 dielectric thickness decreases for the device depicted in Fig. 1. Above the turn-on voltage, devices with different oxide thicknesses exhibit similar EL as a function of the effective injected charge (Supplementary Fig. 17c). Simulated energy-band diagrams elucidate the benefit of reducing the gate oxide thickness at low operating voltages (Fig. 5e). When the gate oxide is thick, the gate capacitance is small and the a.c. voltage swing can only induce gradual band bending at the contacts at low voltage. The reduced quasi-Fermi level splitting and carrier concentrations in the emitter layer lead to low radiative recombination, and the energy bands and carrier concentrations do not reach the expected steady-state condition either. On the basis of these results, we fabricated devices in which a.c. voltage between the CNT network and bottom gate contact is applied across a thin high-*k* gate dielectric (Fig. 5c,d). To reduce parasitics and improve device robustness, we maintained top contact pads on relatively thick SiO_2 (Supplementary Fig. 18). We also found that the use of metallic CNT networks reduces lateral resistive losses at low voltage (Supplementary Fig. 19). The combination of these improvements leads to a reduction in the EL turn-on voltage (V_T) across emitters from infrared to blue wavelengths (Fig. 5g and Supplementary Fig. 20) compared with the earlier result (Fig. 4e). The trend in V_T as a function of EL photon energy closely follows the values calculated from simulation of materials with different band-gap energies, with vertical offset in the data partly attributable to differences in the threshold of photon counts required to determine the onset of EL experimentally. In addition, the EL photon energy is assumed to be the band-gap energy in the simulation whereas the measured photon energy is smaller than the band gap depending on the exciton binding energy of the material. As the photon energy of the emitting material decreases, the total applied voltage swing ($2V_g$) at the onset of EL approaches the photon energy. To further improve device performance, a metal back reflector layer can be incorporated below the emission area to improve light outcoupling, which is degraded as the oxide thickness is reduced. The enhanced EL allows detection at even lower threshold voltages as well as a steeper turn-on characteristic (Fig. 5f). At the voltage at which the 50-nm SiO_2 device starts to turn on (~2.5 V), the 8-nm ZrO_2 device with a back reflector achieves the level of EL that the 50-nm SiO_2 device does not reach until over 5 V. Overall, our results suggest that EL can be produced with a.c. voltages as low as the optical energy gap of the emitting material and on par with the voltages in d.c. electroluminescent devices.

EL spectroscopy and sensing

The presented device we report also enables EL spectroscopy, which can provide material compositional information similar to photoluminescence spectroscopy but without the need for an external light source. This could be especially beneficial for multiplexed material analysis, since photoluminescence spectroscopy requires different excitation wavelengths for different analytes, which involves not only multiple lasers or an intense white light source but also optical path design and filtering to properly extract photoluminescence. We demonstrate the concept and potential of EL spectroscopy by probing a dynamic chemical reaction in solution. The reaction presented in Fig. 6a,b is an imine condensation reaction, which is a type of reaction essential to dynamic covalent chemistry and the synthesis of secondary amines[26]. This reaction can proceed at room temperature with relatively high yield and no byproducts. The reaction between 9-(2-ethylhexyl)carbazole-3,6-dicarboxaldehyde (CDA, **6**) and benzylamine (BA, **7**) to form 9-(2-ethylhexyl)-9H-carbazole-3,6-diyl)bis(*N*-benzylmethanimine) (CDI, **8**) is carried out in a droplet of bis(2-ethylhexyl)benzene covering the EL device (Fig. 6a), which remains in liquid state throughout the measurement. At the beginning of the reaction, CDA gives blue EL (peak at 2.8 eV). With the addition of BA (**7**), the EL of the droplet progressively redshifts and approaches that of CDI (**8**, Fig. 6b). The EL spectrum of the final reaction mixture indicates that the reaction reaches an equilibrium where the reagent and products coexist, which is consistent with the reversible nature of the imine condensation reaction. We believe that the technique of EL spectroscopy can be generalized to study other chemical reactions and analyse mixtures with complex compositions.

With the emitter layer as the top layer, the EL device can also be used as a platform for sensing and studying the structural dynamics of the emitter material. PFO (**1**) is a blue-emitting conjugated polymer commonly used in organic optoelectronics and typically shows additional green EL after some period of device operation[27]. The origin of the green emission is subject to debate and has been correlated with the formation of fluorenone defects or excimers in the polymer chains[27]. Using our EL device, we found that the green emission from a thin PFO (**1**) layer (8 nm, spin-coated from 2.5-mg-ml^{-1} PFO (**1**) in toluene) can be reduced after exposing the device to organic vapours (Fig. 6c–e). This effect can be quantified by the ratio of blue (2.79 eV) and green (2.27 eV) emission and is more pronounced for good solvents of PFO (**1**) (for example toluene and chloroform) compared with poor solvents (for example isopropanol and water, Fig. 6e). These results indicate that configurational changes in the polymer chains play an important role in the appearance of green emission in PFO (**1**), as the vapour of good solvents could facilitate structural rearrangement of the polymer chains but cannot remove fluorenone defects, which involves breaking covalent bonds. Furthermore, the ratio of blue to green emission can be used as a metric for organic-vapour sensing. We demonstrate the feasibility of organic-vapour sensing using chloroform as an analyte, where the blue-to-green ratio of EL increases after 10 s of vapour exposure and decreases to baseline after operating the device for 5 s (Fig. 6f).

Conclusions

We have reported a light-emitting device that can excite EL from a wide variety of materials that emit in the long-wave infrared to ultraviolet wavelength range. By using a porous CNT network as the source contact and applying an a.c. gate voltage, we generate band bending that can overcome carrier-injection barriers in transient

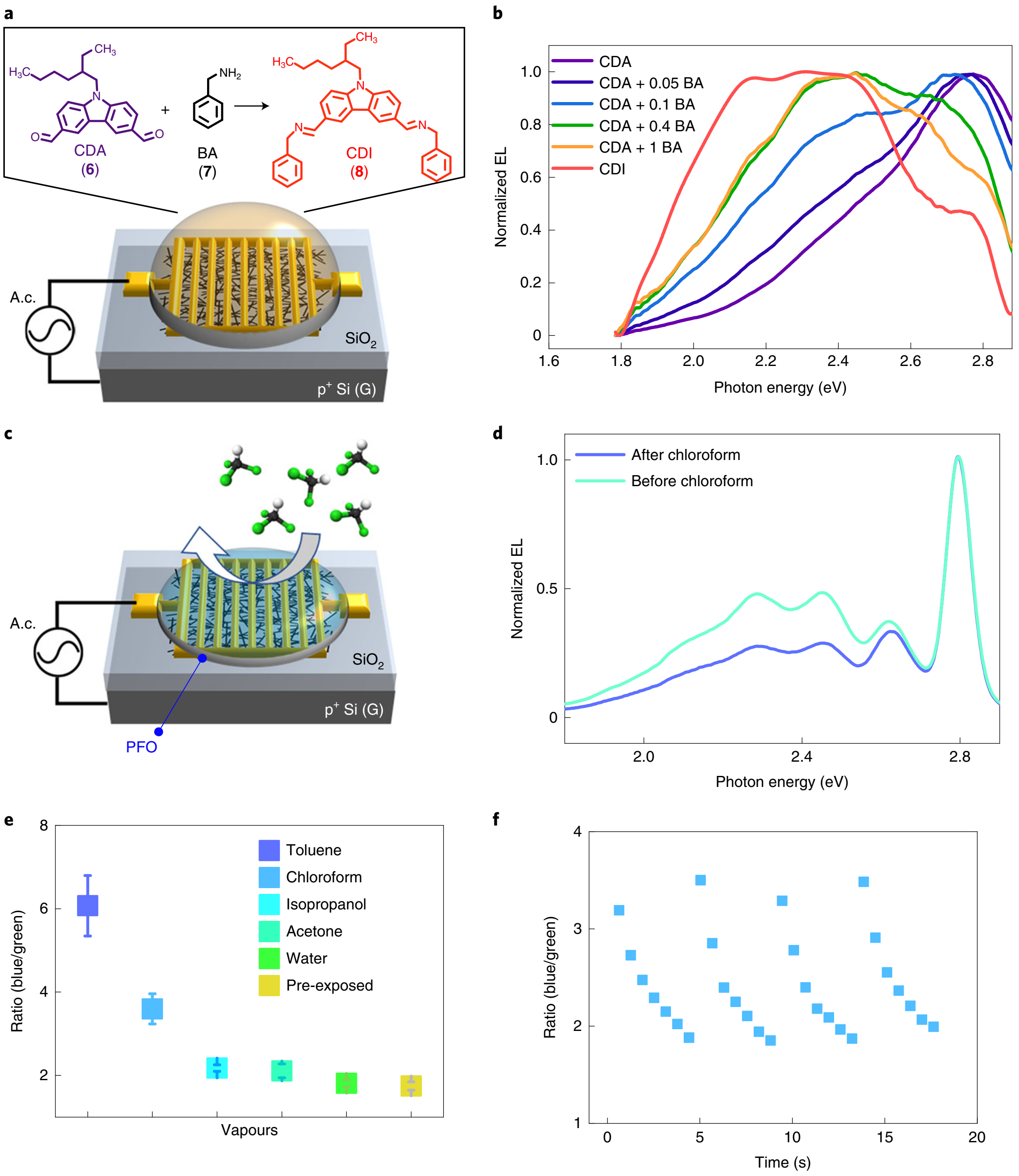

Fig. 6 | EL spectroscopy and sensing. a,**b**, The reaction of CDA (**6**) and BA (**7**) to form CDI (**8**) is carried out in a droplet on the EL device (**a**) and the change in EL spectra reflects progress of the chemical reaction (**b**). **c**,**d**, The EL of an 8-nm PFO layer changes after the device is exposed to chloroform vapour for 10 s (**c**), where the green emission band is substantially reduced (**d**). **e**, The ratio of blue (2.79 eV) to green (2.27 eV) EL after exposure of different solvent vapours, where better solvents of PFO give higher blue-to-green ratios. The error bars correspond to the s.d. of the blue-to-green ratios of three different devices after exposure to the vapours. **f**, Blue-to-green ratio of the PFO device over 5 s after the device is exposed to chloroform vapour for 10 s, with vapour exposure repeated four times.

mode operation and eliminates the need for emitter-specific charge-injection layers. The design allows the emitter layers to be deposited directly on top of the source contact, which lifts limitations on the processability of the light-emitting material. We show that an array of devices can be used to generate multiplexed EL emission, where each emitting material is deposited on one pixel of the array. We also show that the device can be used as a platform for EL spectroscopy and sensing. Our approach creates opportunities for the development of light-emitting devices at extreme wavelengths, as well as the use of EL spectroscopy as a metrology and sensing technique for materials previously inaccessible to this type of analysis.

Methods

Fabrication of devices on Si/SiO$_2$ wafer. The assembly of semiconducting CNTs follows procedures reported in the literature[16]. In brief, 50-nm SiO$_2$/p^{++} Si substrates are washed with deionized water, acetone and isopropyl alcohol, and then treated with O$_2$ plasma for 1.5 min. The substrate is covered by poly-L-lysine solution for 5 min and then washed with water. Semiconducting CNT solution

(99.9% from NanoIntegris) is then drop-casted on the substrate for 30 min and the substrate is washed with deionized water and dried. The density of the CNT network can be tuned by changing the drop-casting time for CNT assembly. The substrate is then annealed under forming gas (5% H_2 in Ar) or nitrogen at 250 °C for 1 h. Source contacts are patterned by photolithography with metal electrodes deposited by electron-beam evaporation. The CNT area is then defined using photolithography and CNTs outside the device area is etched with oxygen plasma.

Fabrication of devices with thin gate dielectric. To improve device robustness and reduce parasitics, we designed the devices such that the top contact/bond pads are situated on top of a thick oxide layer, while the emitting region is situated on a thin oxide layer. The flexible CNT mesh contact allows for continuous electrical connection between the top contact and bottom emitting regions. The fabrication process for the thin-gate-dielectric devices is schematically illustrated in Supplementary Fig. 18. The device with a metal back reflector was used to improve light outcoupling and demonstrate the limits of EL performance at low voltage.

Substrates of 90-nm SiO_2/p^{++} Si are first patterned by photolithography (Heidelberg µPG 101), and the exposed SiO_2 is etched completely away with a 6:1 BOE (buffered oxide etch) until the underlying Si is exposed. (For devices with a metal back reflector, 260-nm SiO_2/p^{++} Si substrates are used instead to accommodate a thick metal back layer; in these devices, a Ti/Ag/Ti (2 nm/150 nm/1 nm) stack is immediately evaporated via electron-beam (Ti) and thermal (Ag) evaporation, followed by liftoff.) Around 8 nm ZrO_2 of gate oxide is deposited by atomic layer deposition (Cambridge Nanotech) at 180 °C. Because neither semiconducting nor metallic CNTs assemble in substantial quantity on the ZrO_2 surface (as determined from atomic force microscopy imaging and electrical measurement), 2-nm SiO_x is evaporated on top of the ZrO_2 to promote assembly of CNT networks. To reduce the parasitic resistance at low voltage, metallic (as opposed to semiconducting) CNTs are used in these devices. The substrate is treated with poly-L-lysine in the same manner, and 99.9% metallic CNT solution (NanoIntegris) is drop-casted on the substrate at 100 °C. After evaporation, the substrate is washed with deionized water. The remainder of the fabrication process (annealing, contact patterning, CNT area patterning) is identical to the general device fabrication procedure described above, where here we used 25-nm Pd contacts. For all devices, a.c. voltage was applied between the top contact and p^{++} Si substrate, which served as a backgate. It is important to note that EL performance depends on the distance between the contact and etched trenches, and this distance should be minimized as much as possible to reduce loss.

Materials and deposition method. Toluene and ethanol were purchased from Sigma Aldrich. Acetone was purchased from VWR. Emitters that are soluble or dispersible in solvents were drop-casted or spin-coated, and the ones that are not soluble were thermally evaporated under high vacuum. The deposition method for each material is listed below.

CdSSe/ZnS alloy quantum dots were purchased from Sigma Aldrich as 1-mg-ml^{-1} toluene solution. For a 0.25-cm^2 chip, 5 µl of solution is drop-casted and dried at room temperature. The substrate is then put in acetone for 1 min, then 1-wt% acetic acid in acetone for 5 min, and finally 1 min in acetone to remove extra ligands from the quantum dots. Only washing with the first step (acetone 1 min) is enough to obtain EL; however, this leads to lower device stability and larger device-to-device variation.

CdSeTe/ZnS quantum dots were purchased from NanoOptical Materials as 5-mg-ml^{-1} toluene solution with excess surfactant. The quantum dots were first washed before deposition: 0.1 ml of the toluene solution was added to 1.5 ml ethanol and the quantum dot precipitates to give a suspension, which is centrifuged at 8,800 r.p.m. for 5 min and the clear supernatant decanted. The quantum dots are then redispersed in 0.2 ml toluene. For a 0.25-cm^2 chip, 5 µl of this solution is drop-casted and dried at room temperature. The substrate is then put in 1-wt% acetic acid in acetone for 5 min, and then 1 min in acetone to remove extra ligands from the quantum dots. Without the initial washing step, drop-casting directly from the initial solution would give a film that cannot be completely dried and appears oily due to excess oleic acid surfactant.

PbS quantum dots were purchased from NNCrystals as a 5-mg-ml^{-1} solution in toluene with excess surfactant. The quantum dots were first washed before deposition: 0.1 ml of the toluene solution was added to 1.5 ml ethanol and the quantum dot precipitates to give a suspension, which is centrifuged at 8,800 r.p.m. for 5 min and the clear supernatant decanted. The quantum dots are then redispersed in 0.2 ml toluene. For a 0.25-cm^2 chip, 5 µl of this solution is drop-casted and dried at room temperature. No subsequent wash was carried out as the quantum dot film would easily delaminate from the substrate while submerged in solution, probably due to the comparatively small size of the quantum dot.

HgTe was synthesized according to the literature method and drop-casted directly on the chip. The quantum dots were washed by dispersing in toluene and precipitating from ethanol three times before deposition to eliminate extra surfactant. For deposition 5 µl of 5-mg-ml^{-1} solution is drop-casted on a 0.25-cm^2 chip and dried at room temperature. Perovskite nanowire was prepared according to the literature method, washed extensively using a centrifuge, decanting the supernatant, and redispersed in hexane. The suspension was drop-casted to give a similar coverage to other inorganic quantum dots; however, the emission from this material is unstable compared with other emitters, only allowing the measurement of its EL spectrum.

All aromatic molecules and conjugated polymers were purchased from Sigma Aldrich. For soluble emitters (all except perylene-3,4,9,10-tetracarboxylic dianhydride; PTCDA), the emitters were dissolved in toluene with 10-mg-ml^{-1} concentration. A volume of 2 µl of this solution is drop-casted on a 0.25-cm^2 chip and dried at room temperature. Drop-casting solution with too high volume leads to long evaporation times and crystallization of the molecules, which could lead to non-uniform EL. PTCDA, due to its very low solubility, was deposited by evaporation under high vacuum and the thickness is 20 nm.

All metal coordination complexes were purchased from Sigma Aldrich except for tris[2-(2,4-difluorophenyl)pyridine]iridium III, which is purchased from Strem Chemicals. $Ru(bpy)_3(PF_6)_2$ was drop-casted from 20-mg-ml^{-1} acetonitrile solution with 2 µl solution dispensed on a 0.25-cm^2 chip. Alq_3 and the two iridium complexes were evaporated to give a 20-nm film due to low solubility. The coordination polymer ZnTCPP was prepared similarly to a literature method,[28] where TCPP was heated in dimethylformamide with an excess amount of zinc acetate for 5 h to give the product as a solid precipitate. (TCPP, 4,4′,4″,4‴-(porphyrin-5,10,15,20-tetrayl)-tetrabenzoic acid; ZnTCPP, the coordination polymer formed by zinc nitrate and TCPP.)

All conjugated polymers were purchased from Sigma Aldrich. These polymers were typically spin-coated at 6,000 r.p.m. at 5-mg-ml^{-1} concentration (toluene solution) or drop-casted from 2.5-mg-ml^{-1} toluene solution with 2 µl solution dispensed on a 0.25-cm^2 chip. The film thickness can be varied by changing the spin speed or concentration (Supplementary Fig. 14), and the thickness dependence of EL for PFO is presented in Supplementary Fig 15.

Electrical and optical characterization. Electroluminescent devices were operated under vacuum at 10 mTorr and EL was collected through a quartz window. The devices were pumped using a bipolar square wave from an Agilent 33522A arbitrary waveform generator applied to the gate electrode, while the source contact was grounded. For voltage above 10 V a voltage amplifier was used with the waveform generator. The EL data presented in this work were measured using a custom-built quantitative micro-photoluminescence instrument described in detail in ref. [29] (Supplementary Information). EL was collected using a ×10 objective lens. EL was dispersed by a spectrometer with a 340-mm focal length and 150-groove-mm^{-1} grating, and detected using a Si CCD (charge-coupled device) (Andor iDus BEX2-DD). Before each measurement, the CCD background was obtained and subsequently subtracted from the EL acquisition. EL of HgTe, which is in the long-wave infrared region, was measured with a Fourier-transform infrared spectrometer. EL of PbS QD, which is in the short-wave infrared region, was measured with a Andor iDus InGaAs camera. Time-resolved EL measurements were collected using a photomultiplier tube connected to an oscilloscope. EL imaging was performed with either a fluorescence microscopy set-up with a CCD detector (Andor Luca) to acquire images, or an Olympus optical microscope with a complementary metal–oxide–semiconductor camera. The emission power was measured using a Thorlabs PM100D power meter with a S120C sensor and cross-calibrated with CCD counts. Transistor I_d–V_g characteristics were taken using an Agilent B1500A semiconductor parameter analyser. For external quantum efficiency measurement (details in following section), a sine wave gate voltage was used and the current was measured by a current amplifier (model SR570, Stanford Research Systems, gain 1 mA V^{-1}) connected to an oscilloscope.

Device simulation. Two-dimensional simulations of the electroluminescent device cross-section were performed using Sentaurus TCAD to understand trends in device behaviour. The simulated device structure consisted of a layer of emissive semiconducting material between two grounded edge contacts 1.4 nm in height, representing two CNTs, situated on top of a 50-nm SiO_2 layer with a gate contact on the bottom. The device width in the third dimension, which corresponds to the length of the CNTs, was 1 µm. The emissive material parameters, intended to roughly represent organic emissive materials, were χ_0 (electron affinity) = 3.3 eV, E_g (band gap) = 2.6 eV, $\varepsilon = 3.5$, μ_n (electron mobility) = μ_p (hole mobility) = 0.001 cm^2 V^{-1} s^{-1}, m_e^* (electron effective mass) = m_h^* (hole effective mass) = m_0. The frequency of the square wave pulse was 50 kHz. For simplicity, the grounded contacts were set to be ambipolar (work function = 4.6 eV) such that emission is equal for upward and downward transitions. The simulation methodology is otherwise similar to that in ref. [15].

Measurement of EQE. The measurement of EQE involves measuring the number of carriers electrically injected into the emitter layer as well as the number of photons emitted. The number of photons emitted is determined from the light output as directly measured by a power meter. For measurement of carrier injection, a sine wave gate voltage is applied to the device, and the time-dependent current is measured by a current amplifier connected in series with the device, that converts the current into a voltage measured by an oscilloscope. The time-averaged charge in each half-cycle is obtained by integrating the current, and the total number of injected carriers is determined from the sum of the magnitudes of the charge from each half-cycle (Supplementary Fig. 13). For an a.c.-driven device with an emitter layer on top, the overall charge is composed of three components: (1) the charge involved in switching the polarity of the capacitor between the metal pad and CNT network contact, (2) the charge entering the emitter layer and (3) the charge exiting the emitter layer. For example, when the gate voltage changes from negative to positive, electrons enter while holes exit the emitter layer. The first component can be determined by measuring the device current without any emitter layer. To estimate the quantum efficiency associated with injection from the CNT contact to the emitter layer, the first charge component is subtracted from the overall measured charge, which yields the sum of electrons injected into the emitter layer and holes exiting the emitter layer. These two components (components 2 and 3) cannot be distinguished, even though the number of carriers injected into the emitter only corresponds to component 2. In our quantum efficiency estimate, we assume that holes do not exit the emitting layer when electrons are injected, and vice versa for electrons during the other half-cycle, thus providing a lower limit for the EQE.

EL spectroscopy of reaction mixture in liquid state. CDA, bis(2-ethylhexyl) benzene and BA were purchased from Sigma Aldrich. CDI was prepared by refluxing CDA with excess BA in ethanol/toluene mixture with a catalytic amount of acetic acid for 5 h. The solvent, catalyst and excess BA were removed under vacuum to give the product CDI as an oily liquid.

For EL spectroscopy of the reaction mixture, 5 μl of bis(2-ethylhexyl)benzene and 5 μl of a toluene solution of CDA (60 mg ml^{-1}) were deposited on the chip of the EL device (same device as Fig. 1, overall chip size 25 mm^2). Bis(2-ethylhexyl) benzene is a high-boiling-point solvent chemically similar to toluene and does not give EL in the range we measure, and the EL of the droplet corresponds to the EL of CDA. All measurements were carried out under vacuum at 20 V and 200 kHz. Under vacuum toluene evaporates, leaving only bis(2-ethylhexyl)benzene, thus the volume of the droplet is unchanged throughout the measurement. Then 5 μl of a toluene solution of BA (1.9 mg ml^{-1}) was added to the droplet, and the droplet gave the EL of CDA + 0.05 BA. With another 5 μl of toluene solution of BA (1.9 mg ml^{-1}) added, the droplet gave the EL of CDA + 0.1 BA, and the EL of reaction mixtures with other compositions can be obtained in a similar manner by adding BA solution of the desired concentration to this droplet.

EL sensing with PFO. PFO (8 nm) was spin-coated from 2.5-mg-ml^{-1} PFO in toluene and the EL device was operated at 12.5 V and 500 kHz for 5 s before exposing to various solvent vapours for 10 s. The EL of the device can then be measured to give the EL spectra after exposure.

Data availability

The data that support the plots within this paper and other findings of this study are available from the corresponding author upon reasonable request.

Received: 12 July 2019; Accepted: 9 July 2020;
Published online: 10 August 2020

References

1. Chao, T.-C. et al. Highly efficient UV organic light-emitting devices based on bi(9,9-diarylfluorene)s. *Adv. Mater.* **17**, 992–996 (2005).
2. Kneissl, M., Seong, T.-Y., Han, J. & Amano, H. The emergence and prospects of deep-ultraviolet light-emitting diode technologies. *Nat. Photon.* **13**, 233–244 (2019).
3. Li, X. et al. Bright colloidal quantum dot light-emitting diodes enabled by efficient chlorination. *Nat. Photon.* **12**, 159–164 (2018).
4. Liu, Y., Li, C., Ren, Z., Yan, S. & Bryce, M. R. All-organic thermally activated delayed fluorescence materials for organic light-emitting diodes. *Nat. Rev. Mater.* **3**, 18020 (2018).
5. Yao, Y., Hoffman, A. J. & Gmachl, C. F. Mid-infrared quantum cascade lasers. *Nat. Photon.* **6**, 432–439 (2012).
6. Pan, Y. et al. Recent advances in alternating current-driven organic light-emitting devices. *Adv. Mater.* **29**, 1701441 (2017).
7. Kong, S. H., Lee, J. I., Kim, S. & Kang, M. S. Light-emitting devices based on electrochemiluminescence: comparison to traditional light-emitting electrochemical cells. *ACS Photon.* **5**, 267–277 (2018).
8. Fresta, E. & Costa, R. D. Beyond traditional light-emitting electrochemical cells—a review of new device designs and emitters. *J. Mater. Chem. C* **5**, 5643–5675 (2017).
9. Cho, S. H. et al. Extremely bright full color alternating current electroluminescence of solution-blended fluorescent polymers with self-assembled block copolymer micelles. *ACS Nano* **7**, 10809–10817 (2013).
10. Jayathilaka, W. A. D. M., Chinnappan, A., Tey, J. N., Wei, J. & Ramakrishna, S. Alternative current electroluminescence and flexible light emitting devices. *J. Mater. Chem. C* **7**, 5553–5572 (2019).
11. Russ, M. J. & Kennedy, D. I. The effects of double insulating layers on the electroluminescence of evaporated ZnS:Mn films. *J. Electrochem. Soc.* **114**, 1066–1072 (1967).
12. Fischer, A. G. Electroluminescent lines in ZnS powder particles: II. Models and comparison with experience. *J. Electrochem. Soc.* **110**, 733–748 (1963).
13. Perumal, A., Lüssem, B. & Leo, K. High brightness alternating current electroluminescence with organic light emitting material. *Appl. Phys. Lett.* **100**, 103307 (2012).
14. Chen, Y. et al. Solution-processable hole-generation layer and electron-transporting layer: towards high-performance, alternating-current-driven, field-induced polymer electroluminescent devices. *Adv. Funct. Mater.* **24**, 2677–2688 (2014).
15. Lien, D.-H. et al. Large-area and bright pulsed electroluminescence in monolayer semiconductors. *Nat. Commun.* **9**, 1229 (2018).
16. Wang, C. et al. Extremely bendable, high-performance integrated circuits using semiconducting carbon nanotube networks for digital, analog, and radio-frequency applications. *Nano Lett.* **12**, 1527–1533 (2012).
17. Sung, J. et al. AC field-induced polymer electroluminescence with single wall carbon nanotubes. *Nano Lett.* **11**, 966–972 (2011).
18. Chen, Y. et al. Effect of multi-walled carbon nanotubes on electron injection and charge generation in AC field-induced polymer electroluminescence. *Org. Electron.* **14**, 8–18 (2013).
19. McCarthy, M. A. et al. Low-voltage, low-power, organic light-emitting transistors for active matrix displays. *Science* **332**, 570–573 (2011).
20. Keuleyan, S., Lhuillier, E. & Guyot-Sionnest, P. Synthesis of colloidal HgTe quantum dots for narrow mid-IR emission and detection. *J. Am. Chem. Soc.* **133**, 16422–16424 (2011).
21. Nobeshima, T., Nakakomi, M., Nakamura, K. & Kobayashi, N. Alternating-current-driven, color-tunable electrochemiluminescent cells. *Adv. Opt. Mater.* **1**, 144–149 (2013).
22. Ahn, J. H., Wang, C., Perepichka, I. F., Bryce, M. R. & Petty, M. C. Blue organic light emitting devices with improved colour purity and efficiency through blending of poly(9,9-dioctyl-2,7-fluorene) with an electron transporting material. *J. Mater. Chem.* **17**, 2996–3001 (2007).
23. Rudmann, H. & Rubner, M. F. Single layer light-emitting devices with high efficiency and long lifetime based on tris(2,2′ bipyridyl) ruthenium(II) hexafluorophosphate. *J. Appl. Phys.* **90**, 4338–4345 (2001).
24. Kang, G.-W., Ahn, Y.-J., Park, D. Y. & Lee, C. Efficient blue electroluminescence from 9,10-diphenylanthracene. *Proc. SPIE* **4800**, 208–215 (2003).
25. Snow, E. S., Novak, J. P., Campbell, P. M. & Park, D. Random networks of carbon nanotubes as an electronic material. *Appl. Phys. Lett.* **82**, 2145–2147 (2003).
26. Jin, Y., Yu, C., Denman, R. J. & Zhang, W. Recent advances in dynamic covalent chemistry. *Chem. Soc. Rev.* **42**, 6634–6654 (2013).
27. Nakamura, T., Sharma, D. K., Hirata, S. & Vacha, M. Intrachain aggregates as the origin of green emission in polyfluorene studied on ensemble and single-chain level. *J. Phys. Chem. C* **122**, 8137–8146 (2018).
28. Zhao, Y. et al. Synthesis of porphyrin-based two-dimensional metal–organic framework nanodisk with small size and few layers. *J. Mater. Chem. A* **6**, 2828–2833 (2018).
29. Amani, M. et al. Near-unity photoluminescence quantum yield in MoS_2. *Science* **350**, 1065–1068 (2015).

Acknowledgements

This work was supported by the Electronic Materials Program, funded by the Director, Office of Science, Office of Basic Energy Sciences, Materials Sciences and Engineering Division of the US Department of Energy under contract no. DE-AC02-05Ch11231. We thank M. Amani, H. Kim and S. Z. Uddin for help with the optical measurement instrument set-up. Work at the Molecular Foundry was supported by the Office of Science, Office of Basic Energy Sciences of the US Department of Energy under contract no. DE-AC02-05CH11231. V.W. acknowledges support from the NSF Graduate Research Fellowship (grant no. DGE-1752814).

Author contributions

Y.Z. and A.J. conceived the idea for the project. Y.Z., D.-H.L. and V.W. carried out optical measurements. V.W. carried out the device simulation. Y.Z. and V.W. fabricated devices and wrote the manuscript. All authors commented on the results and manuscript.

Competing interests

The authors declare no competing interests.

Additional information

Supplementary information is available for this paper at https://doi.org/10.1038/s41928-020-0459-z.

Correspondence and requests for materials should be addressed to A.J.

Reprints and permissions information is available at www.nature.com/reprints.